Journal of Materials Science: Materials in Electronics (2020) 31:8033–8042
https://doi.org/10.1007/s10854-020-03343-5

Investigation of the effect of different Bi_2O_3–x:PVA (x = Sm, Sn, Mo) thin insulator interface-layer materials on diode parameters

Yusuf Badali[1] · Yashar Azizian-Kalandaragh[2,3] · İbrahim Uslu[4] · Şemsettin Altindal[5]

Received: 6 February 2020 / Accepted: 29 March 2020 / Published online: 6 April 2020
© Springer Science+Business Media, LLC, part of Springer Nature 2020

Abstract

In this work, Au/4H–SiC Schottky diodes with different Bi_2O_3–x:PVA (x = Sm, Sn, Mo) thin insulator interface layer were produced for the fabrication of metal/insulator/semiconductor (MIS) structures. The effect of different Bi_2O_3–x:PVA interfacial layer deposited between metal and semiconductor on important optical and electrical parameters of Schottky diodes was investigated. The main electrical parameters of the prepared structures such as the saturation current (I_0), the barrier height (Φ_{B0}), ideality factor (n), and series and shunt resistance (R_s and R_{sh}) were obtained from the I–V characteristics. The discrepancies in these parameters can be ascribed to the use of different nanomaterials as an interlayer. Moreover, the values of n, $\Phi_{B0,}$ and R_s were also extracted by using Cheung and Norde functions and obtained results were compared with each other. The energy dependence of interface states [N_{ss} vs ($E_c - E_{ss}$)] was investigated by taking into account the voltage dependence of $\Phi_e(V)$ and $n(V)$. In addition, Ln(I)–Ln(V) plots were drawn to specify the possible current transport mechanisms of the prepared structures. Experimental results show that the Schottky structures with (Bi_2O_3–Sn:PVA) and (Bi_2O_3–Sm:PVA) interlayers yield higher RR and R_{sh} values and lower I_o values. This provides an evidence to performance increase in MS structures.

1 Introduction

A large number of experimental and theoretical studies have been conducted on metal/semiconductor (M/S) structures, which are obtained as a result of tight contact with a metal and semiconductor at high temperature under vacuum condition. The electrical, dielectric, and optical properties of MS type Schottky barrier diodes (SBDs) are affected by various factors such as applied frequency, doping concentration atoms, interface layer, interface states (D_{it}/N_{ss}), series and shunt resistors (R_s and R_{sh}), sample temperature, and manufacturing processes [1, 2]. To improve the barrier height and performance of MS type SBDs, researchers have used a natural or synthesized thin insulator layer at metal and semiconductor interface [3–9]. Thus, the MS structures are transformed into metal/insulator/semiconductor (MIS) structures. This insulator layer isolates the metal layer from the semiconductor layer, causes significant reduction in the diffusion between these layers and regulates the electrical charge transport. Therefore, such interfacial layer improves the performance and quality of the structure. The homogeneity and the thickness of the insulator layer at M/S interface also have a significant effect on the performance of the structure.

In recent studies, polymer-based MIS structures have attracted significant attention because polymeric insulator layer forms an alternative to traditional insulator layer, such as low dielectric SiO_2, $TiO_{2,}$ and SnO_2, owing to their low cost, easy growth, flexibility, and good performance [10, 11]. Among various polymers that are used as interfacial layer in MS structures, PVA has a good hydrogen bonding systems and chemical properties, non-toxic, water soluble, good technical property, wide crystallinity range, good film formation, low cost, high dielectric resistance (> 1000 kV/mm), and other properties [12–14].

✉ Yusuf Badali
bedeli.yusuf@gmail.com

[1] Department of Electrical & Electronics Engineering, Antalya Bilim University, Antalya, Turkey

[2] Department of Physics, University of Mohaghegh Ardabili, P.O. Box 179, Ardabil, Iran

[3] Department of Engineering Sciences, Sabalan University of Advanced Technologies (SUAT), Namin, Iran

[4] Department of Chemistry Education, Gazi University, Ankara, Turkey

[5] Department of Physics, Faculty of Science, Gazi University, Ankara, Turkey

Bi_2O_3 is one of the major transition metal-oxides in modern semiconductor technology because of its unique important features such as good dielectric properties with ferroelectricity, photoluminescence, and photoconductivity properties as well as its ionic conductivity, bandgap, and reactive index [15–17]. Bi_2O_3 has different phase polymorphism in a way that each phase possesses different physical and optical behavior. Since the predominance of a specific phase depends on the synthesis method, the electrical conductance of Bi_2O_3 can vary up to 5 times, while its bandgap ranges from 2 to 3.96 eV [15–17]. The introduction of such a rich phase polymorphism into the polymeric matrices can alter their chemical, optical, electrical, and dielectric properties and can be used as an interface layer to reduce intermediate-diffusion between metal and semiconductor [18]. Meanwhile, some other studies prove that the use of molybdenum (Mo), samarium (Sm), and tin (Sn) as an interfacial layer in a SBD in the form of oxides or polymer matrix leads to lower ideality factor, low leakage current, and high barrier height [19–23]. In addition, these materials allow the Schottky contact to operate at high temperatures and allow us to perform annealing process at higher temperatures. The dimensions of these doped materials in the nanoscale cause the movement of electrons to be limited.[24–27]. In the literature, there are different methods to make nanoparticles such as thermal evaporation, sol–gel, gamma irradiation, and microwave- and ultrasound-assisted. Among these, the ultrasound-assisted is very easy and low-cost method that has simple compositional control and requires low-temperature procedures and is used extensively in the production of nanostructures [28, 29].

The goal of this study is to investigate the effect of Bi_2O_3–x:PVA (x = Sm, Sn, Mo) nanocomposite interface layers prepared with ultrasound-assisted method on the electrical and optical properties of the Au/n-SiC MS diodes. In line with this goal, firstly the effect of different metal additive (–x) on optical, morphological, and structural behaviors of Bi_2O_3 nanostructures was investigated. Then, the main diode parameters such as series and shunt resistances (R_s and R_{sh}), ideality factor (n), barrier height Φ_{B0}), and surface states (N_{ss}) were explored by using current–voltage (I–V) characteristics.

2 Experimental procedures

2.1 Preparation of Bi_2O_3 nanostructures

Bismuth nitrate [98% $Bi(NO_3)_3{\cdot}5H_2O$; molecular mass 485.07 g/mol], which was used as bismuth source, was purchased from Sigma-Aldrich. First, 0.97 g of bismuth nitrate was dissolved in 20 ml of deionized water to form a 0.1 molar solution of bismuth hydroxide [$Bi(OH)_3$]. The solution obtained was milky and had pH 1. This solution was kept in the ultrasonic bath (28 kHz ± 5%, 100 W) for 30 min. The final solution was centrifuged at 4000 rpm for 5 min to separate the liquid phase from the solid phase and Bi_2O_3 nanostructures were precipitated out. Then Bi_2O_3 nanostructures were washed using distilled water and then thermally treated at 480 °C for 24 h.

2.2 Preparation of Mo-, Sn-, and Sm-doped Bi_2O_3:PVA

Tin dichloride ($SnCl_2$, MW ~ 189.6 g/mol), sodium molybdate dihydrate [$Na_2Mo_{04}{\cdot}2H_2O$; MW ~ 241.9 g/mol], and samarium nitrate hexahydrate [$Sm(NO_3)_3{\cdot}6H_2O$; MW ~ 444.5] were purchased from Sigma-Aldrich. In the original procedure, 0.1 M solution of $SnCl_2$, Na_2Mo_{04} $2H_2O$, and $Sm(NO_3)_3$ $6H_2O$ was prepared by dissolving 0.38 g, 0.48 g, and 0.89 g of these materials in 20 ml double-distilled water, respectively. Bi_2O_3–Mo, Bi_2O_3–Sm, and Bi_2O_3–Sn nanocomposites were obtained by mixing 4 ml of prepared molybdenum, tin, and samarium solutions and pre-prepared 20 ml Bi_2O_3 solution (0.2 M). The rest of the synthesis steps is similar to the previous one. The resulting Bi_2O_3, Bi_2O_3–Mo, Bi_2O_3–Sm, and Bi_2O_3–Sn powders were added to 5 ml of prepared 5% PVA with an amount of 0.1 g and then were mixed in a magnetic stirrer and then in an ultrasonic bath at 80 ºC for 1 h. Thus, these nanocrystals were completely dispersed homogeneously in the polymer.

2.3 Preparation of Au/(Bi_2O_3–x:PVA)/4H–SiC, (x = Sm, Sn, Mo) structures

To prepare Au/(Bi_2O_3–x:PVA)/4H–SiC (x = Sm, Sn, Mo) structures, the n-type 4H–SiC semiconductor substrate with a thickness of (250 ± 25) µm, 7.2×10^{17} cm^{-3} doping-donor atoms (N_D), and 0.012–0.0028 Ω.cm resistivity was purchased from Sigma-Aldrich. First of all, standard chemical cleaning procedure (RCA) was performed to remove impurities and native oxide layers from the 4H–SiC surface. High-purity (99.998%) gold (Au) layer with ~150 nm thickness was deposited whole backside of the 4H–SiC wafer using sputtering at a pressure of ~1.4×10^{-9} Bar and then annealed at 550 °C to achieve a sturdy Ohmic contact. Once the Ohmic contact was achieved, the prepared Bi_2O_3–x:PVA nanocomposites was coated on the top surface of 4H–SiC wafer using spin-coating technique. After this coating process, the high-purity (99.998%) Au circular dots with 1 mm diameter and 150 nm thickness were formed on the (Bi_2O_3–x:PVA) interlayer as rectifying contacts. The I–V characteristics of these prepared samples were performed via a Keithley-2400 source meter whereas Janis-VPF-475 cryostat was used to eliminate noise and light (Fig. 1).

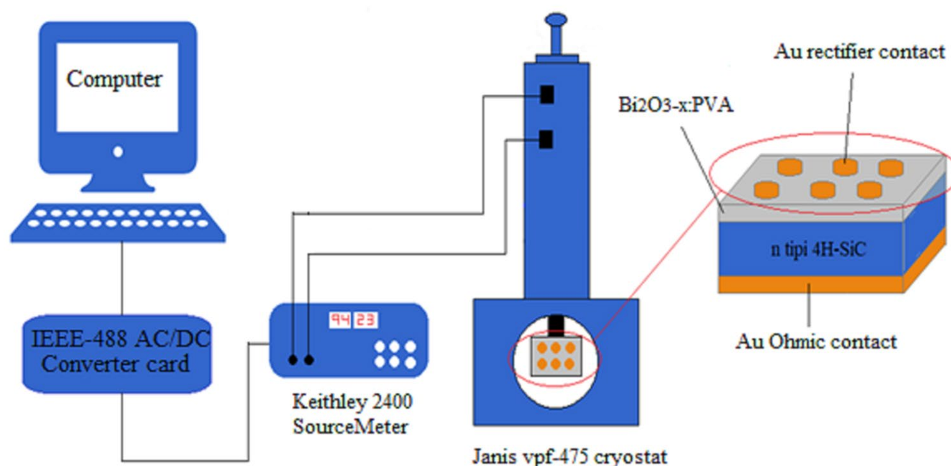

Fig. 1 The schematic of fabricated SBDs and electrical measuring system

3 Results and discussions

3.1 Scanning electron microscopy (SEM) analysis

SEM images of prepared Bi_2O_3, Bi_2O_3–Sm, Bi_2O_3–Sn, and Bi_2O_3–Mo nanostructures are given in Fig. 2a–d. Figure 2a shows that the morphology of pure Bi_2O_3 structures is in the form of inhomogeneous shells with a thickness of about 100–300 nm. Figure 2b shows the SEM image of Bi_2O_3–Sm nanostructures. As seen in this figure, it was found that the crystals of $Bi_{0.62}O_{0.15}Sm_{0.38}$ were formed in spherical structures and settled between the layers of Bi_2O_3.

Figure 2c shows Sn_3O_4 structures consisting of chains with about 70–90 nm diameter which formed in and between the Bi_2O_3 layers. Furthermore, this figure shows that Sn_3O_4 nanostructures are in separate phases and Sn_3O_4/Bi_2O_3 nanocomposites are formed. Figure 2d shows the Mo-doped Bi_2O_3 nanostructures. As seen in this figure, Bi_2MoO_6 crystals are spherical and settled on the Bi_2O_3 layers. SEM images of all samples show that the structures obtained are in the form of large poly-dispersive clusters. In addition, SEM images show that the crystal sizes of all the structures produced are on nanoscale and form a uniform nanocrystal clusters. Variations in surface morphology of the prepared samples are attributed to lattice mismatch, presence of residual oxides, and chemical bonding across the interface.

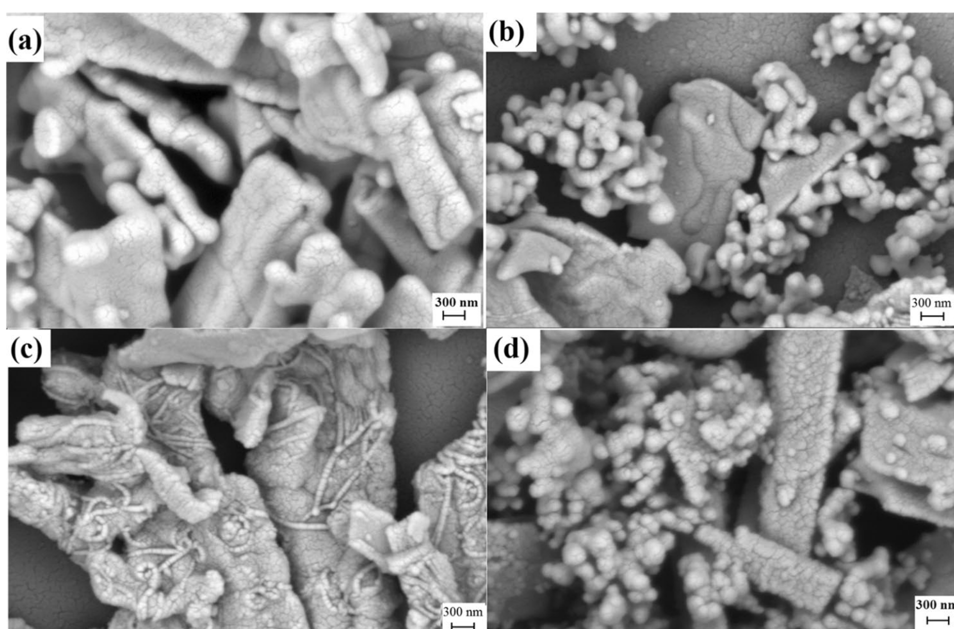

Fig. 2 SEM images of **a** Bi_2O_3, **b** Bi_2O_3–Sm, **c** Bi_2O_3–Sn, and **d** Bi_2O_3–Mo nanostructures prepared by ultrasound-assisted method

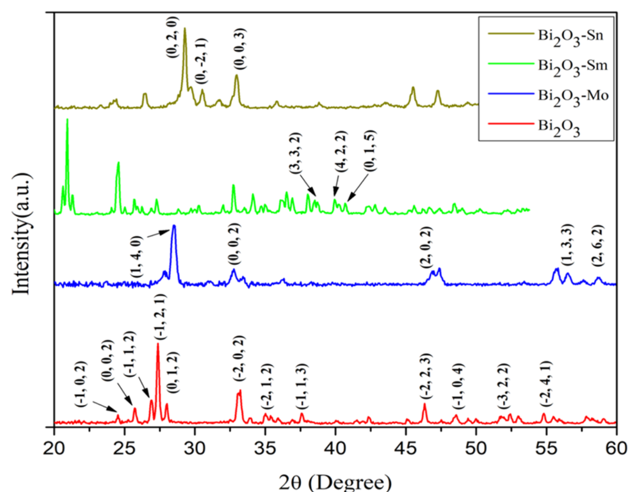

Fig. 3 XRD pattern of prepared Sm-, Sn-, and Mo-doped Bi_2O_3 nanostructures

3.2 X-ray diffraction

The structural properties of Bi_2O_3 and molybdenum-, samarium-, and tin-doped Bi_2O_3 were also explored using the X-ray diffraction (XRD) with a Cu Kα ($\lambda = 1.5406$ Å) radiation with range of 2θ from 20 to 80. Figure 3 shows the XRD pattern of the samples that are prepared using ultrasound-assisted method. The diffraction pattern can be well indexed to monoclinic phase Bi_2O_3 reported in ICDD Card (No. 27–0053). In this pattern, the peaks belong to planes (− 1, 0,2), (0, 0, 2), (− 1, 1, 2), (− 1, 2, 1), (0, 1, 2), (− 2, 0, 2), (− 2, 1, 2), (− 1, 1, 3), (− 1, 2, 3), (− 2, 2, 3), (− 1, 0, 4), (− 3, 2, 2), and (− 2, 4, 1). These peaks clearly show that Bi_2O_3 nanostructures were fabricated in the form of monoclinic crystal structure and the space group *P*21/*c* [31]. The average crystalline size of Bi_2O_3 nanostructures was found approximately 37 nm using Debye–Scherrer equation (Eq. 1);

$$D = k\lambda/\beta\cos\theta, \quad (1)$$

where *D*, *k*, *λ*, *β,* and *θ* are the size of the crystallite, Scherrer constant value (~ 0.9), the X-ray wavelength, the full-width at half-maximum of diffraction peak (FWHM), and the Bragg diffraction angle, respectively [32].

The XRD results of molybdenum-doped Bi_2O_3 showed that the diffraction pattern could be well indexed to orthorhombic phase Bi_2MoO_6 reported in ICSD Card (No. 72–1524). In this pattern, the peaks correspond to the planes (1, 4, 0), (0, 0, 2), (2, 0, 2), (1, 3, 3), (0, 8, 2), and (2, 6, 2). Therefore, Bi_2MoO_6 nanostructures were fabricated in the form of orthorhombic crystal structure and the space group 61 [33]. The average crystalline size of Bi_2MoO_6 nanostructures was found approximately 27 nm. The XRD results of samarium-doped Bi_2O_3 showed that the diffraction pattern could be well indexed to cubic phase $Bi_{0.62}O_{0.15}Sm_{0.38}$ reported in ICSD Card (No. 85–2251). In this pattern, the peaks correspond to the planes (3, 3, 2), (4, 2, 2), and (0, 1, 5). Thus, it was concluded that $Bi_{0.62}O_{0.15}Sm_{0.38}$ nanostructures were fabricated in the form of cubic crystal structure and the space group 1213 [34]. The average crystalline size of $Bi_{0.62}O_{0.15}Sm_{0.38}$ nanostructures was found approximately 32.6 nm. The XRD results of tin-doped Bi_2O_3 show that the diffraction pattern peaks correspond to the planes (3, 3, 2), (4, 2, 2), and (0, 1, 5), which leads to the conclusion that Sn_3O_4 nanostructures are of anorthic crystal structure and the space group *P** [35]. The average crystalline size of Sn_3O_4 nanostructures was found approximately 29.8 nm.

3.3 UV–visible spectroscopy

Absorbance spectrum of the Bi_2O_3 and molybdenum-, samarium-, and tin-doped Bi_2O_3 nanostructures was obtained using a UV-1800 Shimadzu UV–vis absorption spectrophotometer and the bandgap values of these nanostructures were obtained from the data in Fig. 4. The bandgap energy (E_g) values of the prepared nanostructures are obtained using the following equation:

$$\alpha h\nu = c\left(h\nu - E_g\right)^m. \quad (2)$$

In this relation, absorption coefficient (α) is related to the energy of photon ($h\nu$), *c* is a constant proportional, and *m* is the power factor ($m = 0.5$ for the direct transition) [36]. The

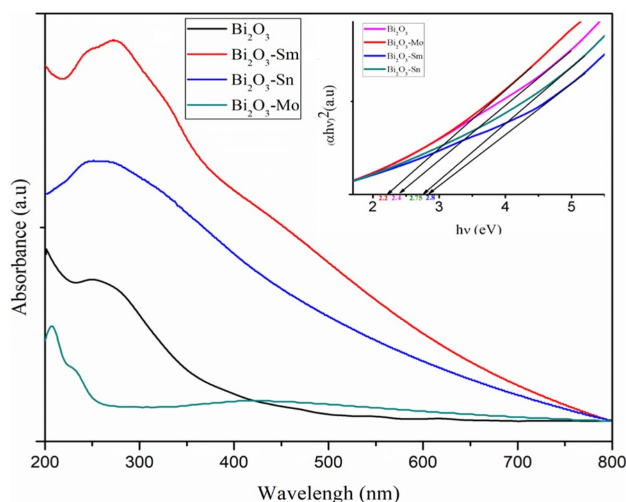

Fig. 4 UV–visible absorption spectrum of prepared Sm-, Sn-, and Mo-doped Bi_2O_3 nanostructures

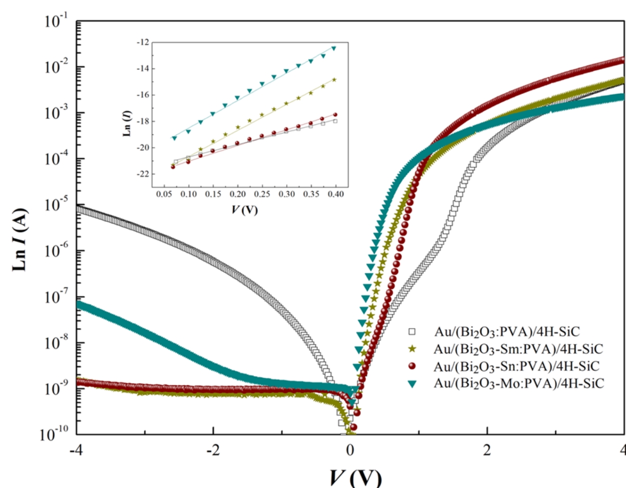

Fig. 5 The semi-logarithmic I–V characteristics of Au/(Bi_2O_3–x:PVA)/4H–SiC structures

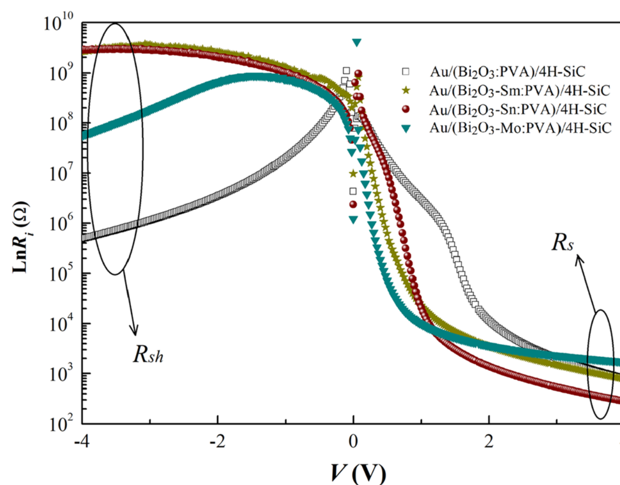

Fig. 6 The LnR_i–V characteristics of Au/Bi_2O_3–x:PVA/4H–SiC structures

direct bandgap energy (E_g) value is evaluated by extrapolating the straight line part of $(\alpha h\nu)^2$ versus ($h\nu$) curves as shown in the Fig. 4. E_g values of Bi_2O_3 and Mo-, Sm-, and Sn-doped Bi_2O_3 were obtained 2.4, 2.2, 2.75, and 2.8 eV, respectively.

3.4 Electrical characterization

For the prepared Au/Bi_2O_3–x–PVA/4H–SiC (x = Sm, Sn, Mo) samples, Figure 5 shows a comparison of the semi-logarithmic forward- and reverse-bias I–V characteristics. The values of reverse saturation current (I_0) and zero-bias barrier height (Φ_{B0}) were obtained from the y-intercept of LnI vs V plot whereas those of ideality factor (n) were extracted using the slope values of the linear parts this plot [37]. As shown in Fig. 5, the LnI vs V plots are linear at low bias regions, but there occurs deviation from the linearity at high forward-bias voltages because of the effect of R_s and interface states. The resistance–voltage (R_i–V) profile of the Au/Bi_2O_3–x–PVA/4H–SiC structures was obtained by using Ohm's law at ± 4 V as follows:

$$R_i = \partial V / \partial I. \tag{3}$$

Figure 6 shows that the R_i values of all Au/Bi_2O_3–x–PVA/4H–SiC samples reach to minimum at high forward-bias voltages due to the effect of R_s. However, the R_i can reach maximum values at high reverse-bias voltages due to the effect of R_{sh} [9–11].

Also, the diodes are characterized by their rectifying ratio (RR), which is the rate between current for positive and negative electrical bias (= I_F/I_R at ± 4 V). The measurement results confirm a major decline in R_s and leakage current values (increase in R_{sh}) for the Au/Bi_2O_3–Sn:PVA/4H–SiC and Au/Bi_2O_3–Sm:PVA/4H–SiC structures in comparison with other samples. Therefore, high values of RR (9.98×10^6 and 3.34×10^6) and R_{sh} values (2.77×10^9 and 2.55×10^9 Ω) of the structures with Bi_2O_3–Sn:PVA and Bi_2O_3–Sm:PVA interfacial layer, respectively, suggest that these structures are almost an ideal Schottky diode. These results show that the diodes with Sn- and Sm-doped interlayer would perform better compared to the ones with pure Bi_2O_3 and Mo-doped PVA interlayers. This is believed to be a result of addition of Sm and Sn materials to Bi_2O_3 nanostructures which passivates many of the N_{ss} or dislocations and increases the barrier height (BH) and dielectric constant.

If MS or MIS/MPS structures or SBDs have R_s effect and therefore n becomes greater than one ($n > 1$), the relation between the forward V ($V > 3kT/q$) and I values can be explained via the standard TE theory [9–11]:

$$I = I_0 \exp\left(\frac{qV}{nkT}\right)\left[1 - \exp\left(\frac{-qV}{kT}\right)\right]. \tag{4}$$

In Eq. 4, k is the Boltzmann constant and T is temperature on the Kelvin scale. The value of $I_0$is the reverse-bias saturation current given by Eq. 5 [38, 40].

$$I_0 = AA^* T^2 \exp\left(\frac{-q\Phi_{B0}}{kT}\right). \tag{5}$$

In Eq. 5, A is the diode area, A^* is the Richardson constant and is 143 A/cm^2 K^2 for 4H–SiC [16], and Φ_{B0} is the apparent BH ($\Phi_{app.}$) at $V = 0$. The values of n were determined from the linear region slope of LnI–V plots using followin g equation:

Table 1 The obtained electrical parameters of Au/Bi_2O_3–x:PVA/4H–SiC structures

Structures	I_0(A)	n	Φ_{B0} (eV)	R_s(Ω)	R_{sh} (Ω)	RR
Au/(Bi_2O_3:PVA)/4H–SiC	7.77×10^{-5}	4.08	0.57	777	4.69×10^{5}	6.03×10^{2}
Au/(Bi_2O_3–Sm:PVA)/4H–SiC	2.47×10^{-9}	1.95	0.84	763	2.55×10^{9}	3.34×10^{6}
Au/(Bi_2O_3–Sn:PVA)/4H–SiC	6.39×10^{-6}	3.23	0.65	277	2.77×10^{9}	9.98×10^{6}
Au/(Bi_2O_3–Mo:PVA)/4H–SiC	4.23×10^{-9}	2.00	0.82	1691	5.40×10^{7}	3.19×10^{4}

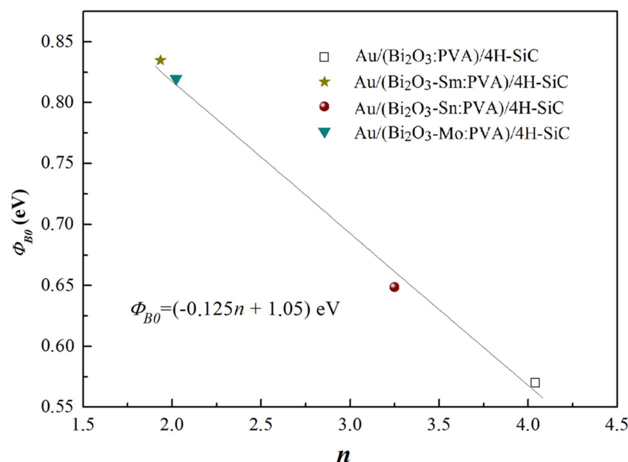

Fig. 7 The Φ_{B0} versus n plot of Au/Bi_2O_3–x:PVA/4H–SiC structures

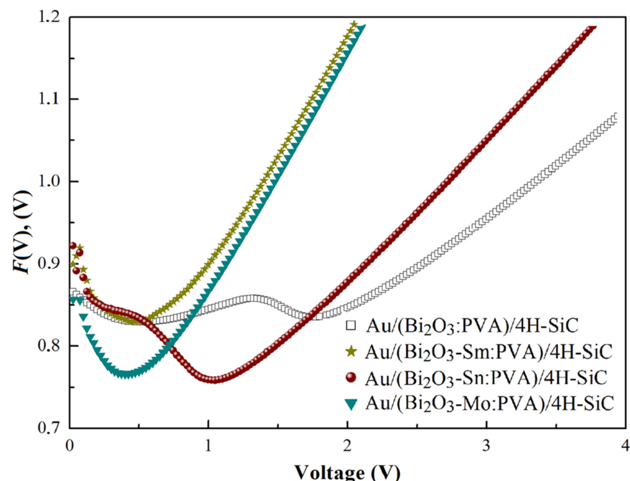

Fig. 8 The $F(V)$–V characteristics of the Au/Bi_2O_3–x:PVA/4H–SiC structures

$$n = \frac{q}{kT}\left(\frac{\mathrm{d}V}{\mathrm{d}(\mathrm{Ln}I)}\right) \tag{6}$$

The value of Φ_{B0} was calculated using the experimental values of I_0 and A using Eq. 5. Table 1 shows the experimental values of I_0, n, Φ_{B0}, R_s, $R_{sh,}$ and RR for each sample. The obtained results indicate that these parameters are a powerful function of the interlayer structures. The higher values of n for Au/Bi_2O_3–PVA/4H–SiC attributed greatly to the existence of structural defects, organic interfacial layer, inhomogeneity of BH, and the existence of N_{ss}between interlayer and 4H–SiC. The higher values of ideality factors for Au/(Bi_2O_3:PVA)/4H–SiC structure correspond to the lower BHs and RR (Table 1). Furthermore, there is a good linear relation between Φ_{B0} and n as ($\Phi_{B0} = -0.125n + 1.05$) eV (Fig. 7). Such behavior can be associated with the wide distribution of lower BHs or patches, also the N_{ss} at semiconductor and at organic layer interface. The value of mean barrier height (Φ_{B0}) was found as 0.92 eV for the ideal case ($n = 1$).

Electrical parameters of SBDs could be obtained via several methods which vary due to difference of measurement conditions such as bias voltage and measurement system [39, 42]. Therefore, it is often that some parameters, such as BH, ideality facto,r and R_s, of the SBDs show dependence on the applied bias voltage as well as the methods utilized for measurements and calculation. Moreover, the accuracy and reliability of calculations might be reduced due to very narrow linear section in LnI–V plots. In order to overcome these problems, a new method was developed by Norde and utilized by researchers for the extraction of BH and R_s for the case of $n = 1$ [41–43]. Later, Bohlin [44] modified this method for the case of $n > 1$ as follows:

$$F(V) = \frac{V}{\gamma} - \frac{kT}{q}\left[\mathrm{Ln}\left(\frac{I(V)}{AA^{*}T^{2}}\right)\right]. \tag{7}$$

In Eq. 7, γ is a dimensionless quantity which is larger than n. Therefore, $F(V)$ values for the Au/Bi_2O_3–x:PVA/4H–SiC structures were calculated using Eq. 7 and $F(V)$ vs V curves of these structures were represented in Fig. 8. It is obvious that these curves for all SBDs have a local minimum point [$F(V_0)$] thus R_s and Φ_B are extracted from I–V data using the following equations:

$$R_s = \frac{kT(\gamma - n)}{qI_0}, \tag{8}$$

$$\Phi_B = F(V_o) + \frac{V_o}{\gamma} - \frac{kT}{q}. \tag{9}$$

In Eqs. 8 and 9, V_0 and I_0 are the bias voltage and current values that correspond to the minimum point of the

Table 2 Some diode parameters obtained from Norde functions

Structures	F_{min}(V)	V_{min}(V)	I_{min} (A)	Φ_B(eV)	R_s (Ω)
Au/(Bi_2O_3:PVA)/4H–SiC	0.84	1.75	5.58×10^{-5}	1.09	944
Au/(Bi_2O_3–Sm:PVA)/4H–SiC	0.83	0.89	2.50×10^{-5}	1.11	1006
Au/(Bi_2O_3–Sn:PVA)/4H–SiC	0.76	1.19	17.4×10^{-5}	0.98	239
Au/(Bi_2O_3–Mo:PVA)/4H–SiC	0.77	0.72	3.62×10^{-5}	0.87	714

$F(V_0)$ in $F(V)$ vs V curve. Using these values in Eqs. 8 and 9, R_s and Φ_B of Au/Bi_2O_3–x:PVA/4H–SiC structures were extracted and presented in Table 2. Observations showed that the values of BH and R_s calculated using the Norde method are higher than those calculated using TE theory for two type structures. Some observed discrepancies in the BH and R_s obtained from TE and Norde theory are associated with bias voltage and the nature of the method used.

The basic electrical parameters of the fabricated MPS structures such as n, Φ_B, and R_s values were also calculated using the Cheung's functions as an alternative way. In order to derive the Cheung functions, the I_0 from Eq. 4 must be replaced and logarithm of both sides must be taken as follows:

$$V = \left(\frac{nkT}{q}\right)\mathrm{Ln}\left(\frac{I}{AA^*T^2}\right) + n\Phi_B + IR_s \tag{10}$$

Therefore, equation is obtained and from here I. Cheung function is derived from [42],

$$\frac{dV}{d(\mathrm{Ln}I)} = \left(\frac{nkT}{q}\right) + IR_s \tag{11}$$

In addition, if both sides of Eq. 10 become equal with $H(I)$,

$$H(I) = V - \left(\frac{nkT}{q}\right)\mathrm{Ln}\left(\frac{I}{AA^*T^2}\right), \tag{12}$$

$$H(I) = n\Phi_B + IR_s. \tag{13}$$

II. Cheung functions are obtained as mentioned above [42]. The dV/d(LnI) and H(I) versus I curves of the different Au/(Bi_2O_3–x:PVA)/4H–SiC MPS structures were obtained using Eqs. 11 and 12 and given in Fig. 9a–d. These figures show that the dV/d(LnI) vs I and H(I) vs I curves of all structures have good linear behavior. Thus, the values of n, Φ_B, and R_s for fabricated MPS type structures were obtained from the slope and y-intercept point and are presented in Table 3. There are some differences between the obtained values from Cheunge and Norde methods (Tables 2, 3). These results showed that the voltage region has a significant effect on the values of basic electrical parameters and therefore must be taken into account. In other words, both the ideality factor and the barrier height vary significantly with voltage. In the high forward-bias voltage region, the resistance of the structure corresponds to the actual series resistance. While R_s is dominant at high forward-bias voltages, the N_{ss} is predominant in medium voltage regions.

In general, n and Φ_{B0} are calculated using TE theory since Ln(I) vs V curves yield a linear region at low forward-bias region. On the other hand, these parameters show dependence on bias voltage as in Eqs. 10 and 11 for the bias voltages after the linear region. Therefore, R_s and N_{ss} show dominance in different voltage regions such that the former dominates in the downward of the I–V curve whereas the latter dominates at the low and intermediate bias voltage ranges. Moreover, N_{ss} exhibits a distribution profile and its distribution within the bandgap energy can be obtained using the following equations [45]:

$$\Phi_e = \Phi_{B0} + \alpha(V) = \Phi_{B0} + \left(1 - \frac{1}{n(V)}\right)V, \tag{14}$$

$$n(V) = \frac{qV}{kT\mathrm{Ln}(I/I_0)} = 1 + \frac{\delta}{\varepsilon_i}\left[\frac{\varepsilon_s}{W_D} + qN_{ss}(V)\right], \tag{15}$$

where Φ_e, $\alpha(V)$, ε_s, ε_i, and W_D are the voltage--dependent effective BH, the changing in the BH with applied bias voltage [$\alpha(V) = d\Phi_e/dV$], the permittivity of semiconductor material, the permittivity of polymeric layer material, and the depletion layer width which may be computed from the reverse-bias C^{-2} vs V curve at high frequency. The energies of N_{ss} (E_{ss}) with respect to conduction band edge (E_c) for n-type semiconductors are express as [45] follows:

$$E_c - E_{ss} = q(\Phi_e - V). \tag{16}$$

In the MIS or MPS structures, the interfacial layer thickness is usually higher than 30 Å; therefore, the surface states are completely governed by semiconductor. As a result, the charges at surface states are in-equilibrium with semiconductor. Thus, the energy-dependent profile of N_{ss} is deduced by Card and Rhoderick as follows [45]:

$$N_{ss}(V) = 1/q\left[\varepsilon_i/\delta(n(V) - 1) - \varepsilon_s/W_D\right]. \tag{17}$$

In Eq. 17 δ is the thickness of interface layer. Therefore, the N_{ss} density distribution profiles for prepared structures

Fig. 9 dV/d(LnI)–I and $H(I)$–I curves of **a** Au/(Bi_2O_3:PVA)/4H–SiC, **b** Au/(Bi_2O_3–Sm:PVA)/4H–SiC, **c** Au/(Bi_2O_3–Sn:PVA)/4H–SiC, and **d** Au/(Bi_2O_3–Mo:PVA)/4H–SiC structures

Table 3 Some diode parameters obtained from the Cheung's functions

Structures	dV/d(LnI)–I		H(I)–I	
	R_s (Ω)	n	R_s (Ω)	Φ_B (eV)
Au/(Bi_2O_3:PVA)/4H–SiC	154	18.3	143	0.60
Au/(Bi_2O_3–Sm:PVA)/4H–SiC	89	31.6	86	0.53
Au/(Bi_2O_3–Sn:PVA)/4H–SiC	106	17.7	101	0.54
Au/(Bi_2O_3–Mo:PVA)/4H–SiC	586	28.8	569	0.53

were obtained by using I–V data in Eqs. 16 and 17 and given in Fig. 10.

The value of N_{ss} increased from nearly the middle of the bandgap energy of SiC towards the bottom of E_c (Fig. 10). The tail of curves in Fig. 10 for N_{ss} was attributed to the deep-level density of N_{ss} in the near bandgap energy of semiconductor. Figure 10 shows that the value of N_{ss} for Au/(Bi_2O_3–x:PVA)/4H–SiC (MPS) structures with x = Sm and Sn is quite lower than that for Au/

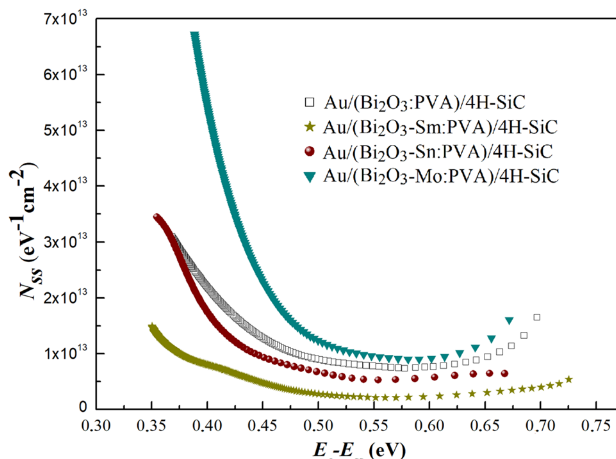

Fig. 10 The energy density distribution profile of the Au/(Bi_2O_3–x:PVA)/4H–SiC structures

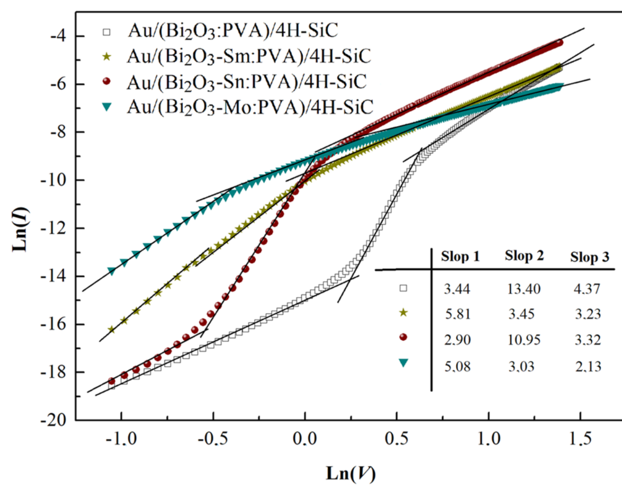

Fig. 11 Double-logarithmic *I–V* characteristics of Au/Bi_2O_3–*x*:PVA/4H–SiC structures

(Bi_2O_3:PVA)/4H–SiC structures. Such behavior of the N_{ss} confirmed that adding the Sm and Sn into Bi_2O_3:PVA interfacial layer leads to increased performance due to the decrease of the average value of N_{ss}. This enhancement is also associated with particular density distribution of the N_{ss} and their re-ordering and re-structuring under bias voltage.

Double-logarithmic Ln(*I*)−Ln(*V*) curves are plotted and given in Fig. 11 to determine the possible transmission mechanisms in the correct bias region. As seen in Fig. 11, these curves yield three linear regions with different slopes for each sample. These regions will be referred as low (slope 1), medium (slope 2), and high (slope 3) voltage regions. If the obtained slope values are close to 1, the current transmission mechanism can be explained by Ohm's law. In addition, if these slopes are greater than 2, the current mechanism can be explained by space charge-limited current (SCLC) and if the slopes are larger than these values, the trap charge-limited current (TCLC) can dominate in current mechanism. As shown in Fig. 11 and the table in it, almost all slope values are considerably higher than 2. Therefore, TCLC appears to be more dominant current transport mechanism rather than SCLC. In other words, the current transport is provided by the TCLC mechanism, especially at medium and high forward biases ($V > 2$). In this mechanism, increased number of injected charges causes filling of the N_{ss} or traps and this in turn increases in the space charge [39, 40]. Moreover, high slope values can be associated with the distribution of trap states located below the Fermi level.

4 Conclusion

The structural, optical, and electrical parameters of the prepared Au/Bi_2O_3–*x*–PVA/4H–SiC (*x* = Sm, Sn, Mo) (MPS) structures were characterized by various methods. The bandgap energy of Bi_2O_3 and Mo-, Sm-, and Sn-doped Bi_2O_3 was obtained as 2.4, 2.2, 2.75, and 2.8 eV, respectively. The important diode parameters such as *n*, $\Phi_{B,}$ and R_s values were obtained from Ohm's law, Norde, and Cheung functions for all structures and were compared with each other. A good linear relation between Φ_{B0} and *n* was ascribed to the existence of organic layer (Bi_2O_3–*x*:PVA), the wide distribution of low barrier height, and also the N_{ss} at semiconductor and at organic layer interface. Energy distribution profile of interface states [N_{ss} vs ($E_c - E_{ss}$)] was obtained by taking into account the *I–V* results, voltage-dependent barrier height [$\Phi_e(V)$], and ideality factor [$n(V)$]. In addition, Ln(*I*)−Ln(*V*) curves were plotted to determine the possible current transmission mechanism of the prepared structures. The experimental results showed that the electrical parameters are greatly affected by the doped nanomaterials. These results also showed that the Au/Bi_2O_3–*x*–PVA/4H–SiC samples show a good performance in terms of diode parameters. These results indicated that especially (Bi_2O_3–Sm–PVA) and /(Bi_2O_3–Sn–PVA) interfacial polymer layer lead to the increase in quality or performance of the structure rather than conventional insulator layer with low dielectric permittivity such as SiO_2, SnO_2, and Si_3N_4.

Acknowledgements This study was supported by Gazi University Scientific Research Project. (Project Number GU-BAP.05/2019–26).

References

1. M. Shah, M.H. Sayyad, K.S. Karimov, Electrical characterization of the organic semiconductor Ag/CuPc/Au Schottky diode. J. Semicond. **32**, 1–4 (2011)
2. Y. Zhou, C. Liu, S. Fan, Schottky contact of an artificial polymer semiconductor composed of poly(dimethylsiloxane) and multiwall carbon nanotubes. J. Mater. Chem. A **3**, 319539 (2015)
3. S. Altındal Yeriskin, The investigation of effects of (Fe_2O_4–PVP) organic-layer, surface states, and series resistance on the electrical characteristics and the sources of them. J. Mater. Sci. Mater. Electron. **30**, 17032–17039 (2019)
4. Ç.Ş. Güçlü, A.F. Özdemir, Ş. Altindal, Double exponential I-V characteristics and double Gaussian distribution of barrier heights in (Au/Ti)/Al_2O_3/n-GaAs (MIS)-type Schottky barrier diodes in wide temperature range. Appl. Phys. A **122**, 1032–1038 (2016)
5. P.R. Reddy, V. Janardhanam, I. Jyothi, S.H. Yuk, V.R. Reddy, J.C. Jeong, S.N. Lee, C.J. Choi, Modification of Schottky barrier properties of Ti/p-type InP Schottky diode by polyaniline (PANI) organic interlayer. J. Semicond. Technol. Sci. **16**, 664–674 (2016)
6. A.R.V. Roberts, D.A. Evans, Modification of GaAs Schottky diodes by thin organic interlayers. Appl. Phys. Lett. **86**, 072105 (2005)

7. F.J. Willars-Rodríguez, I.R. Chávez-Urbiola, R. Ramírez-Bon, P. Vorobiev, YuV Vorobiev, Effects of aluminum doping in CdS thin films prepared by CBD and the performance on Schottky diodes TCO/CdS:Al/C. J. Alloy Compd **817**, 152740 (2020)
8. S. Altındal-Yerişkin, M. Balbaşı, I. Orak, The effects of (graphene doped-PVA) interlayer on the determinative electrical parameters of the Au/n-Si (MS) structures at room temperature. J. Mater. Sci. Mater. Electron. **28**, 14040–14048 (2017)
9. M.A.M. Ahmed, W.E. Meyer, J.M. Nel, Effect of (Ce, Al) co-doped ZnO thin films on the Schottky diode properties fabricated using the sol–gel spin coating. Mater. Sci. Semicond. Process. **103**, 104612 (2019)
10. V.R. Reddy, Electrical properties of Au/polyvinylidene fluoride/n-InP Schottky diode with polymer interlayer. Thin Solid Films **556**, 300–306 (2014)
11. O. Vural, Y. Safak, S. Altindal, A. Turut, Current–voltage characteristics of Al/Rhodamine-101/n-GaAs structures in the wide temperature range. Curr. Appl. Phys. **10**, 761–765 (2010)
12. N. Baraz, İ. Yücedağ, Y. Azizian-Kalandaragh, S. Altındal, Determining electrical and dielectric parameters of dependence as function of frequencies in Al/ZnS–PVA/p-Si (MPS) structures. J. Mater. Sci. Mater. Electron. **28**, 1315–1321 (2017)
13. Ç. Bilkan, Y. Azizian-Kalandaragh, Ş. Altındal, R. Shokrani-Havigh, Frequency and voltage dependence dielectric properties, AC electrical conductivity and electric modulus profiles in Al/Co_3O_4–PVA/p-Si structures. Physica B **500**, 154–160 (2016)
14. C.V.S. Reddy, X. Han, Q.Y. Zhu, L.Q. Mai, W. Chen, Dielectric spectroscopy studies on (PVP +PVA) polyblend film. Microelectron. Eng. **83**, 281–285 (2006)
15. M. Zdujić, D. Poleti, C. Jovalekić, L. Karanović, Mechanochemical synthesis and electrical conductivity of nanocrystalline d-Bi_2O_3 stabilized by HfO_2 and ZrO_2. J.Serb. Chem. Soc. **74**, 1401–1411 (2009)
16. T. Kimoto, J.A. Cooper, *Fundamentals of Silicon Carbide Technology*, 1st edn. (Wiley, Singapore, 2014)
17. E.M. Waleed, A.A. Al-Ghamdi, Electrical and mechanical properties of bismuth oxide nanowire/poly(vinyl acetate). J. Appl. Polym. Sci. **118**, 1598–1605 (2010)
18. W. Li, Facile synthesis of monodisperse Bi_2O_3 nanoparticles. Mater. Chem. Phys. **99**, 174–180 (2006)
19. M. Gökçen, T. Tunc, Enhancement of dielectric characteristics of polyvinyl alcohol (PVA) interfacial layer in Au/PVA/n-Si structures by Bi_2O_3 disperse. J. Appl. Ceram. Technol. **10**, 64–69 (2013)
20. V. Manjunath, V.R. Reddy, S.P.R. Reddy, V. Janardhanam, C.J. Choi, Electrical and frequency-dependent properties of Au/Sm_2O_3/n-GaN MIS junction with a high-k rare-earth Sm_2O_3 as interlayer. Curr. Appl. Phys. **17**, 980–988 (2017)
21. H. Park, C.R. Helms, Thermal stability of molybdenum–silicon nitride–silicon Schottky diodes. J. Appl. Phys. **69**, 3149–3153 (1991)
22. G. Kano, M. Inoue, J.I. Matsuno, S. Takayanagi, Molybdenum–silicon Schottky barrier. J. Appl. Phys. **37**, 2985–2987 (1996)
23. L. Stöber, J.P. Konrath, F. Patocka, M. Schneider, U. Schmid, Controlling 4H–SiC Schottky barriers by molybdenum and molybdenum nitride as contact materials. IEEE Trans. Electron Device **63**, 578–583 (2016)
24. E. Simoen, C. Claeys, V.B. Neimash, A. Kraitchinskii, N. Krasko, O. Puzenko, A. Blondeel, P. Clauws, Deep levels in high-energy proton-irradiated tin-doped n-type Czochralski silicon. Appl. Phys. Lett. **76**, 2838–2842 (2000)
25. Y. Azizian-Kalandaragh, F. Sedaghatdoust-Bodagh, A. Habibi-Yangjeh, Ultrasound-assisted preparation and characterization of β-Bi_2O_3 nanostructures: Exploring the photocatalytic activity against rhodamine B. Superlattice Microstruct. **81**, 151–160 (2015)
26. K.T. Al-Rasoul, I.M. Ibrahim, I.M. Ali, R.M. Al-Haddad, Synthesis, structure and characterization of ZnS QDs and using it in photocatalytic reaction. J. Sci. Technol. Res. **3**, 213–217 (2014)
27. P. Saha, T.P. Majumder, S.C. Debnath, Ultraviolet–visible and photoluminescence spectroscopy of newly synthesized CdSe nanostructures. Int. J. Eng. Sci. Innov. Technol. **3**, 86–91 (2014)
28. Y. Azizian-Kalandaragh, Investigation of optical and structural properties of sonochemically prepared 3-mercaptopropionic acid capped bismuth sulfide nanostructures. Optoelectron. Adv. Mater. Rapid Commun. **10**, 201–204 (2016)
29. J.H. Bang, K.S. Suslick, Applications of ultrasound to the synthesis of nanostructured materials. Adv. Mater. **22**, 1039–1059 (2010)
30. M.I. Díez-García, V. Manzi-Orezzoli, M. Jankulovska, S. Anandan, P. Bonete, R. Gómez, T. Lana-Villarreal, Effects of ultrasound irradiation on the synthesis of metal oxide nanostructures. Phys. Procedia **63**, 85–90 (2015)
31. Z. Cui, J. Liu, D. Zeng, H. Liu, C. Xie, Quasi-one-dimensional bismuth tungsten oxide nanostructures templated by cotton fibers. J. Am. Ceram. Soc. **93**, 1479–1483 (2010)
32. B. Lamia, Étude du système CeO_2–Bi_2O_3 pour applications catalytiques et conductimétriques, PhD Dissertation, Université de Toulon France, 2011
33. M. Lutz, S.E. Pratsinis, Bismuth oxide nanoparticles by flame spray pyrolysis. J. Am. Ceram. Soc. **85**, 1713–1718 (2002)
34. F. Pertlik, J. Zemann, Neubestimmung der kristallstruktur des Köchlinits. Fortschr. Miner. Beih. **60**, 162–163 (1982)
35. W. Akiteru, Preparation of a new phase having a cation-ordered C-type rare-earth oxide related structure in the systems Bi_2O_3–Ln_2O_3 (Ln= Sm, Eu, Gd, Tb, and Dy). J. Solid State Chem. **120**, 32–37 (1995)
36. F. Lawson, Tin oxide–Sn_3O_4. Nature **215**, 955–956 (1967)
37. H. Paramita, S. Shyamal, H. Mandal, P. Fageria, S. Pande, C. Bhattacharya, Photocatalytic activity of Bi_2O_3 nanocrystalline semiconductor developed via chemical-bath synthesis. Electrochim. Acta **123**, 494–500 (2014)
38. E. Arslan, S. Butun, Y. Şafak, H. Uslu, I. Taşcıoğlu, Ş. Altındal, E. Ozbay, Electrical characterization of MS and MIS structures on AlGaN/AlN/GaN heterostructures. Microelectron. Reliab. **51**, 370–375 (2011)
39. J.C. Wiemneri, Electrical characterization of 4H- and 6H–silicon carbide Schottky diodes, Thesis, Master of Science in Engineering Physics, USA, 1995
40. S.M. Sze, *Physics of Semiconductor Devices*, 2nd edn. (Wiley, New York, 1981)
41. H.J. Norde, A modified forward I-V plot for Schottky diodes with high series resistance. J. Appl. Phys. **50**, 5052–5053 (1979)
42. S.K. Cheung, N.W. Cheung, Extraction of Schottky diode parameters from forward current–voltage characteristics. Appl. Phys. Lett. **49**, 85–87 (1986)
43. E.H. Nicollian, *MOS (Metal Oxide Semiconductor) Physics and Technology* (Wiley-Interscience, New York, 2002)
44. K.E. Bohlin, Generalized Norde plot including determination of the ideality factor. J. Appl. Phys. **60**, 1223–1224 (1986)
45. H.C. Card, E.H. Rhoderick, Studies of tunnel MOS diodes I. Interface effects in silicon Schottky diodes. J. Phys. D **4**, 1589–1601 (1971)

Publisher's Note Springer Nature remains neutral with regard to jurisdictional claims in published maps and institutional affiliations.